CHEN BINGQIAN
and
LU YIJIE

Monitoring of residual subsidence in old goafs based on ultrashort-baseline InSAR technology

When applying the differential interferometric synthetic aperture radar (D-InSAR) technology to high-resolution SAR data, an external digital elevation model (DEM) with comparable resolution is usually not available for removing topography-related phase component for the purpose of deformation extraction. To avoid the problem due to insufficient DEM resolution, a DEM-free InSAR approach based on ultrashort spatial baselines (USB) is introduced here, capable of overcoming DEM limitations of conventional differential InSAR technique. We analyzed the principle of selection of USB interferometric pairs, and briefed permanent scatter (PS) pixel phase modeling and parameter estimation with respect to USB technology. This method was applied to the subsidence monitoring in three old goafs in Yulin mining, Shaanxi. The corresponding law of subsidence obtained was used to establish the empirical relation between circulating peak of subsidence velocity and mining thickness as well as between subsidence velocity cycle and ratio of mining depth to mining thickness. The experiment results provide basis for predicting and evaluating the residual subsidence of old goafs.

Keywords: *old goaf, residual subsidence, ultrashort baseline, InSAR, subsidence monitoring*

1. Introduction

The residual deformation in old goafs denotes residual movement and deformation of rock strata and the ground surface as a response to stress redistribution of the unbalanced rock system caused by the effect of ground stress, external force, rock material strength attenuation, etc [1-8]. Despite the small magnitude, it features elusiveness, complexity, suddenness and sustainability in comparison with strata deformation during mining. It is the frequent resultant accidents that render residual subsidence monitoring noticeable, albeit rare due to constraints on labor force and finance. In order to acquire the change law of past subsidence, the subsidence and deformation data should be accessible, which is beyond the scope of conventional measurement methods but instead can and only can be realized by interferometric synthetic aperture radar (InSAR) technology. Therefore, research findings of theories and technologies of InSAR-based deformation monitoring in old goafs are of great theoretical and pragmatic significance to the formation of movement & deformation monitoring theories and stability evaluation methods.

Jung monitored Gaeun goaf conditions by using persistent scatterer InSAR (PS-InSAR), and found that the maximum amount of subsidence is 11.2cm and that the average subsidence velocity measured in fracture development zone reaches up to 0.5 cm/yr [9]. Gueguen employed Differential InSAR (D-InSAR) and persistent scatterer interferometry (PSI) to monitor 1992-2007 subsidence in an old goaf and achieved the result of a good fit with the result acquired by conventional measurement methods. He found that the residual subsidence velocity peaks at 1.25cm/yr 5-7 years after mining (i.e. 1992-1997) and then levels off [10]. Fan Hongdong et al. used D-InSAR in combination with measured data to monitor the subsidence in a Xuzhou old goaf and obtained the deformation law as a result [11-12].

The resolutions of SAR images captured by newly-launched radar satellites (TerraSAR-X, Sentinel-1A, ALOS-2) are increasingly lifted from previous medium resolution (around 20m) to meter level and submeter level. Consequently, the gradients of deformation monitoring rise up towards the identification of a broadened variety of surface features, accompanied by the demand for higher resolution and precision of externally derived digital elevation model (DEM). In the light of differential interferometry, both the conventional D-InSAR technology and recently formed time-series SAR technology are applied on the precondition that external DEMs can remove topographic phases. Problems may arise from lack of matching DEM. For example, the most popular global SRTM data, acquired in 2000 by NASA, has such parameters as 30m or so horizontal precision, 10m-16m or so vertical precision and 30m-90m resolution [13-14]. If differential interferometry utilizes these DEM data to remove topographic fringes of high-resolution SAR images, the estimation result of deformation parameters may be erroneous. To overcome these limitations, Liu Guoxiang et al. proposed the ultrashort spatial baselines (USB)

Messrs. Chen Bingqian and Lu Yijie, School of Geography & Geomatics and Urban-Rural Planning, Jiangsu Normal University, No. 101, Shanghai road, 221116, Xuzhou, China. Email: bqccumt@gmail.com

technology. With spatial baseline thresholds, SAR images are separated into different interferometric pairs before permanent scatter (PS) pixels are extracted and used for time-series deformation modeling [15]. The shorter the spatially perpendicular baseline, the longer the topographic height needed to produce a fringe of phase change. Ultrashort spatial baseline can be defined as the one on whose basis the interferogram is not sensitive to topographic effects with minor changes of phase. Thus, an external DEM is no longer required for USB-based differential processing, which decreases the number of parameters to be estimated by solution and estimates parameters with greater robustness.

2. Procedures of usb-based insar technology

2.1 SELECTION OF USB-BASED INTERFEROMETRIC PAIRS

The topographic phase contribution is modulated in the interferograms that are used for InSAR-based subsidence detection, which is a major concern for selecting the reasonable interferometric pairs. The longer the spatial baseline, the more topographic phases contribute to interferometric fringes. The conventional differential processing generally utilizes an external DEM of the imaged surface to remove the topographic fringes from the interferograms. For the high resolution SAR images, it is however a challenging task to obtain a matching DEM for removing topographic effects. It is a reasonable way to choose the interferometric pairs with USBs for minimizing topographic effects without needing an external DEM.

The threshold of USB can be derived by analyzing the functional relation between elevation error and the ground motion along radar line of sight (LOS). Assuming that the height error of the DEM used for differential processing is Dh, the error Dl in the resultant LOS motion can be expressed as [16]

$$\Delta l = \frac{B_{\perp}}{R\sin\theta}\cdot\Delta h \qquad \ldots 1$$

Where B^ denotes the perpendicular baseline length of an interferometric pair,q the radar look angle, and R the sensor-to-surface distance (i.e., slant range). It is clear that the contribution of the height error onto the LOS motion is proportional to both B⊥ and Δh. Fig.1 shows the LOS motion error Δl as a function of B⊥ and Δh for the case of TerraSAR-X (TSX) system with the nominal imaging parameters, i.e., θ = 41°, R = 662520 m. It reveals that a TSX interferometric pair with B⊥ of less than 15 m generates a USB interferogram that is less sensitive to topographic effects.

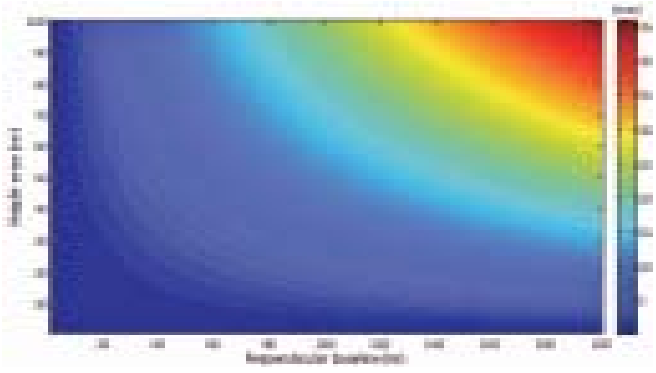

Fig.1 The LOS motion error is represented as a function of the perpendicular baseline length and the height error

As a summary, TSX interferograms with spatial baselines of less than 15 m are less sensitive to topographic effect, so that unnecessary of the use of an external DEM for differential interferometry. Therefore, the spatial baseline of 15m becomes the threshold for selection of USB interferometric pairs.

2.2 PS PIXEL IDENTIFICATION AND NETWORKING

PS detection is the key to the USB technology by supporting the subsequent establishment and analysis of the time-series deformation model. PS selection in most research papers is guided by the PS detection method proposed by Ferretti et al., i.e. ADI-based PS detection [17]. As this method takes PS pixel stableness into account and ignores the characteristic of strong scattering, it is easy to lead to wrong results. Allowing for the steadiness and scattering of surface feature spectrum, we connect time series parameters (including correction coefficients, amplitudes and amplitude discretion indices (ADIs)) in series to detect PS pixels more accurately. Specifically speaking, correction coefficients and amplitudes are first employed to exclude seriously decorrelated pixels and pixels of weak return signals; then, PS pixels are determined by ADIs according to the steadiness of pixel amplitude.

According to Document [18], the correlation measure γ reflects the level of interferometric phase noise calculated for SAR images. The selection of PS pixels is inspired by it. During actual calculation, in terms of a particular resolution cell, the estimation formula of γ can be based on the information of neighboring pixels within a certain surrounding scope, i.e.

$$\gamma = \frac{\left|\sum_{i=1}^{m}\sum_{j=1}^{n} M(i,j)S^{*}(i,j)\right|}{\sqrt{\sum_{i=1}^{m}\sum_{j=1}^{n}\left|M(i,j)\right|^{2}\sum_{i=1}^{m}\sum_{j=1}^{n}\left|S(i,j)\right|^{2}}} \qquad \ldots 2$$

Where *M* and *S* are pixel information (complex number) blocks of two SAR images as interferometric pairs, * denotes complex conjugate operator. Generally speaking, the larger the γ (between 0 and 1)is, the lower the interferometric phase noise is.

Also, the time series of correlation coefficient of an arbitrary resolution cell in overlapped image areas can be computed: $\gamma_1, \gamma_2 \ldots, \gamma_N$o. Before searching alternative PS pixels, it is necessary to compute the mean time-series correlation coefficient pixel by pixel, i.e.

$$\overline{\gamma} = \sum_{k=1}^{N} \gamma_K \quad \text{... 3}$$

Meanwhile, we take into consideration echo strength or pixel amplitude. Assuming there are N+1 images, the amplitude threshold is set according to

$$\begin{cases} \overline{A_i} = \dfrac{\sum_{k=1}^{N+1} A_{k\_i}}{N+1} \\ \overline{A_i} \geq A_{thres} \end{cases} \quad \text{... 4}$$

In which A_i is the mean amplitude of pixel *i* in time-series images, A_{thres} is the amplitude threshold, A_{k_i} is the amplitude of pixel i in the kth image. We use equation (3) to generate a suitable threshold *T*, and subsequently extracts pixels with mean correlation coefficients larger than *T* (i.e. $\gamma \geq T$). Meanwhile, the pixel amplitude threshold A_{thres} is determined according to equation (4) and used for searching for targeted pixels of strong echo information. Through equation (3), the scope necessary for PS selection is greatly shrunk with the exclusion of much-decorrelated pixels, and thus the computation efficiency is improved. Test analysis result shows that pixels located at vegetated areas can be well removed when T=0.25, which is a necessity because radar reflection in this locality is vulnerable to unpredictable external disturbance such as vegetation growth and leaves rustling in wind. Equation (4) erases pixels of week reflection signals including watershed (specular reflection) and shadowy areas when A_{thres}=1.2 as an example.

Please be noted that the correlation coefficient is controlled by the dimension of the estimation window (as shown in Equation 2). The larger the window dimension is, the higher the estimator accuracy is, but the lower the resolution is. In general, using estimation windows, single but effective PS pixels can hardly be identified, and unstable pixels near identified PS pixels may be wrongly regarded as PS pixels. In addition, the echo strength of many hard targets which may be initially strong will change at the end of the time series over time (such as diminishing or being destroyed). The use of equation (4) in such cases may mistake these targets as PS pixel targets. Given this, it is unreliable to merely rely on the value and amplitude of correlation coefficients to identify effective PS pixels. To this end, to refer to other non-correlation coefficient information is a must to the refined selection of PS pixels. In this paper, we determine PS pixels in the final step by employing ADI technique.

The ADI-based PS pixel estimation takes advantage of the steadiness of pixel amplitude rather than the correlation, during which the strength of each in-area pixel is analyzed in time series towards steady scatterers. According to the research findings by Ferretti et al., when ADI<0.25, the standard phase error approximates ADI, i.e. [19]

$$\sigma_v = DA \quad \text{... 5}$$

Hence, D_A can be seen as the alternative measurement parameters of phase stability. By setting the threshold of D_A, our criterion of selection of targeted PS pixels is

$$D_A < D_T \quad \text{... 6}$$

In which D_T is amplitude dispersion threshold. Due to our previous measure that the pixels have been initially sieved by using time-series correlation coefficient method and amplitude method, the condition that ADI should be used on the premise of high performance-to-noise ratio has been achieved.

After PS pixels are determined, we continue on to networking and the establishment of differential phase model by using the commonly-sued Delaunay irregular triangular network. For details of networking, please refer to references [20-23].

2.3 PS PHASE MODELING AND PARAMETER ESTIMATION

We assume that the sum of N SAR images is obtained in the study area in a particular time. Consequently, M USB-based interferometric pairs are formed according to the USB principle, whose corresponding temporal baseline is t_i(*i*=1, 2, ……, *M*). Thus, the PS phase $\phi(x, t_i)$ in the ith interferogram can be expressed as

$$\phi(x,t_i) = \varphi_d(x,t_i) + \varphi_a(x,t_i) + \varphi_n(x,t_i) \quad \text{... 7}$$

Where $\varphi_d(x,t_i)$, $\varphi_a(x,t_i)$ and $\varphi_n(x,t_i)$ represent the phase components of the respective relative ground movement, the atmospheric effect, and the decorrelated noise in between two imaging periods. For the USB interferometric pairs introduced herein, the topographic phase component is negligible.

Supposing that linear deformation is the major form of deformation in the study area, thus the deformation phase can be seen as the function of vertical deformation velocity, time baseline and the inflection angle of radar angles. In terms of the time array of N SAR photos, there exist *N*-1 consecutive time intervals $(\xi_1, \xi_2, \ldots, \xi_{N-1})$ and the corresponding *N*-1 vertical deformation velocities. Thus, the vector of the vertical deformation velocity of an arbitrary PS can be given as

$$V_x = [\mathrm{v}_x^1, \mathrm{v}_x^2, \ldots, \mathrm{v}_x^{N-1}]^T \quad \text{... 8}$$

We let the kth SAR image be combined with the Ith image to produce the ith ($1 \leq i \leq M$) interferogram ($1 \leq k < l \leq N$). Then, the deformation phase in equation (7) is represented by

$$\underset{1\times M}{\varphi_d(x,t_i)} = \underset{1\times M}{g(t_i)} \cdot \underset{M\times 1}{V_x} \quad \text{... 9}$$

Where

$$g(t_i)_{1\times M} = [0\,0\cdots 0\,0\;\beta(\xi_k)\;\beta(\xi_{k+1})\;\cdots\beta(\xi_{l-1})\;\;0\cdots 0] \quad \ldots 10$$

Where can be expressed as

$$\beta(\xi_j) = \frac{4\pi}{\lambda}\cdot\cos\theta\cdot\xi_j \qquad (k \le j \le l-1) \quad \ldots 11$$

In which γ is the radar wave length, θ is the inflection angle of the radar wave. Equation (7) can be developed as

$$\phi(x,t_i) = g(t_i)\cdot \mathrm{V}_x + \omega(x,t_i) \quad \ldots 12$$

Where $\omega(x,t_i)$ is the residual phase, which is the sum of the phase component of the atmospheric effect and the one of the decorrelated noise. In terms of the ith differential interferogram, the increment in the interferometric phase along an arbitrary arch section is expressed as

$$\Delta\phi(x,y,t_i) = \mathrm{g}(t_i)\cdot\Delta \mathrm{V}_{x,y} + \Delta\omega(x,y,t_i) \quad \ldots 13$$

In which $\Delta\omega(x,y,t_i)$ denotes the residual phase increment, which is the sum of the phase component incredent of the atmospheric effect and the one of the decorrelated noise between a pair of PS pixels, and $\Delta V_{x,y}$ is the vector of the vertical deformation velocity increment, which is defined as

$$\Delta V_{x,y} = [\Delta \mathrm{v}^1_{x,y}\;\;\Delta \mathrm{v}^2_{x,y}\;\cdots\;\Delta \mathrm{v}^{N-1}_{x,y}]^T \quad \ldots 14$$

Where

$$\Delta \mathrm{v}^j_{x,y} = v^j_y - v^j_x \qquad (1\le \mathrm{j} \le \mathrm{N}-1) \quad \ldots 15$$

For the arch section connecting *x* and *y*, a pair of randomized PS pixels, M equations similar as equation (15) can be listed with M interferometric pairs, and expressed in matrix as

$$\Delta\phi(x,y,t_i)_{N\times 1} = A_{N\times M}\cdot V_{M\times 1} + W_{N\times 1} \quad \ldots 16$$

In which *A* represents the coefficient matrix of $\beta(\xi_j)$ and zero value, $\Delta\phi$ is the phase increment vector, *W* is the residual phase increment vector. Their formulas are

$$A = [\beta(\xi_k)\;\;\beta(\xi_{k+1})\;\cdots\;\beta(\xi_{l-1})\;\;0\cdots 0] \quad \ldots 17$$

$$W = [\Delta w(\mathrm{x},\mathrm{y},\mathrm{t}_1)\;\;\Delta w(\mathrm{x},\mathrm{y},\mathrm{t}_2)\;\cdots\;\Delta w(\mathrm{x},\mathrm{y},\mathrm{t}_M)]^T \quad \ldots 18$$

For equation (16), the deformation velocity can be estimated by using the weight least-square adjustment:

$$\Delta\hat{V}_{x,y} = A(\mathrm{A}^T\mathrm{P}^{dd}\mathrm{A})^{-1}\mathrm{A}^T\mathrm{P}^{dd}\,\Delta\phi \quad \ldots 19$$

Where Pdd represents the priori weight matrix obtained by inversing the variance-covariance matrix of phase increment. Please be noted that when M<N-1, the matrix ATPddA is singular matrix. The pseudo-inverse matrix obtained by singular value decomposition algorithm can displace the said matrix in that case, so that ensuring unimpeded parameter solution-seeking. For the details of USB time-series modeling, please refer to references [15-16].

3. Experiment

3.1 A BRIEF INTRODUCTION OF THE STUDY AREA

The study area is three old goafs in Yuyang coal mine area in Yuyang district of Yulin city, Shaanxi. Yuyang coal mine is exploited officially by Shaanxi Coal Industry Ltd., a subsidiary of China Energy Technology Holdings Ltd. Yuyang has a continental, monsoon-influenced semi-arid climate, bordering Yulin Yuyang Airport to the west, and Yulin Desert Park to the east. Villages like Suanpitan, Xiaojiahuochang, and Changjiehan are under this district. Up to now, Yuyang coal mine has the mining right for 13.0258 square km mining fields and the mineral exploitation right for 237.32 square km mining fields.

The mine exploration area in this test covers Goaf 2301, Goaf 2302 and Goaf 2304, whose adjacent working face locations are shown in Fig.2. All of them were exploited from west to east at the uniform depth of 200m and the thickness of about 3.38m using fully caving method. Each neighboring working face was 45m far from each other. The sizes of 2301, 2302, and 2304 working faces were 1,100×200m, 1,120m×175m, and 950m×190m, respectively. The exploration work for them was independently completed in March 25th, 2008, Feb. 25th, 2009 and Sep.25th, 2009, respectively.

$$A = [\Delta\phi(\mathrm{x},\mathrm{y},\mathrm{t}_1)\;\;\Delta\phi(\mathrm{x},\mathrm{y},\mathrm{t}_2)\;\cdots\;\Delta\phi(\mathrm{x},\mathrm{y},\mathrm{t}_M)]^T$$

Fig.2 Plane map of working face locations

3.2 EXPERIMENTAL DATA

The encompassing SAR data used for this test are derived from the 25-scene TSX satellite data in German Aerospace Center, spanning 308 days (from August 30, 2012 to July 4, 2013). The images are high-resolution and HH co-polarized at the initial distance resolution of 0.9m and the azimuth resolution of 0.8m. The time span of most neighboring data points is 11 days, and 22 days for a few neighboring data points. The characteristics of high resolution and short time span is conducive to the subsequent selection of PS pixels. In this section, we employ the said USB technique to set limits to the length of spatial baselines to ensure that only interferometric pairs of less than 15m baselines are considered in this test. According to Figs.3 and 4, a sum of 27 interferometric pairs satisfies our requirements, among which the absolute value of the longest spatial baseline is 14.45m and the shortest spatial baseline is 1.05m. The shortest temporal baseline is 11 days, and the longest temporal baseline is 209 days.

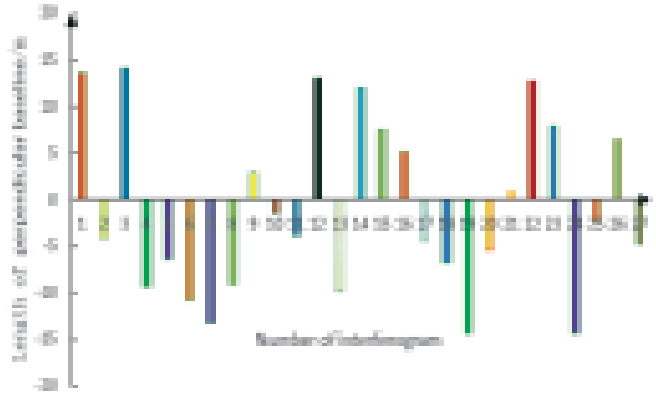

Fig.3 Distribution of spatially vertical baselines

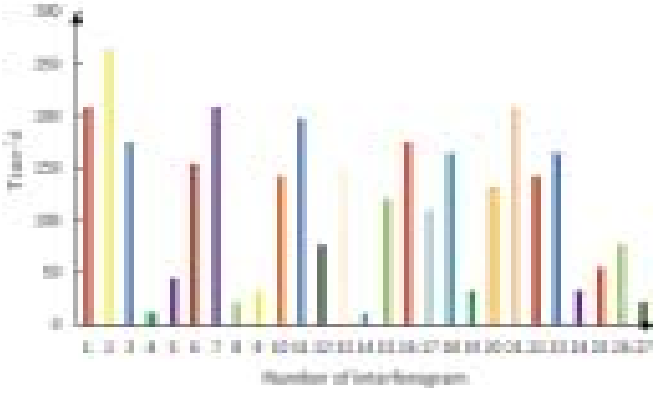

Fig.4 Distribution of temporal baselines

3.3 EXPERIMENTAL RESULTS

There are 134,507 effective PS pixels detected by us with the proposed method in Section 2.2, which are marked in yellow in Fig.5. As can be seen in it, PS pixels are at a high density of about 20,000 per square km. Areas in buildings and roads witness a particular high density of PS pixels, serving as favorable PS pixel targets with steady radar backscatter. As a contrast, PS pixels are much less dense in farming fields and vegetated areas, because of highly season-varying ground reflections different with a second plough, the change of soil water content, crop growth and leaves rustling in wind as examples. In addition, the high resolution of TRX SAR images allows identification of more details and characteristics of surface features, which further magnifies more and finer targeted pixels.

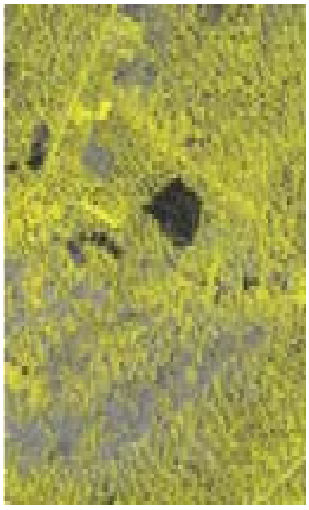

Fig.5 Distribution of PS pixels

For PS pixels detected before, by using the said USB-based approach to deformation velocity solutions, we let a relatively steady PS pixel in the research area as the reference pixel (marked in red crisscross in Fig.6) and accordingly calculate the deformation speed of PS pixels. Fig.6 shows the map of subsidence velocity distribution of all PS pixels in research area (already been geologically encoded). Fig.7 is the enlarged drawing of subsidence velocity distribution of all PS pixels in the triple of old goafs. As shown in Fig.6, there are all together four noticeable deformed localities (A, B, C, D) with uneven subsidence in the study area, and the maximum deformation velocity is up to 120mm/a. Locality B has the strongest deformation, followed by locality A and locality C.

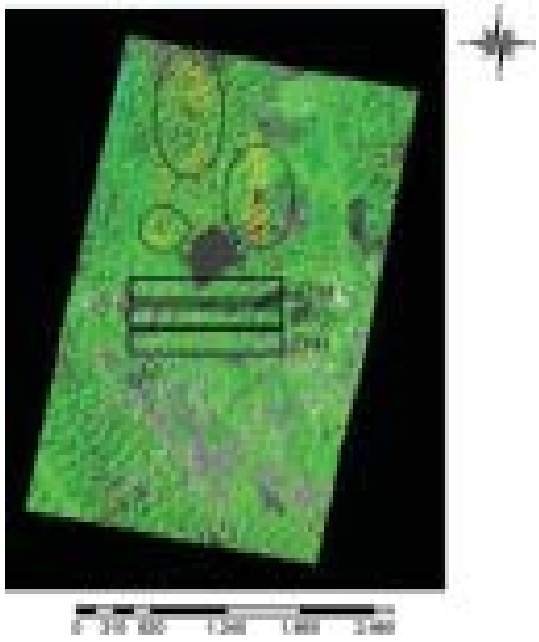

Fig.6 The map of subsidence velocity distribution of all PS pixels in research area

Locality B is locally deformed. According to relative miners, exploitation work is under way beneath B and D by using the fully-caving method and the filling exploration method, respectively. Corresponding protective coal pillars are left in site. As a result, subsidence in B is much greater than that in D. As their ores are just finished recovered, A and C suffer small residual deformation.

Fig.7 shows that the areas on top of 2301, 2302 and 2304 working faces tend to stabilized. By calculating the deformation speed of PS pixel targets in the working faces, we obtain the maximum subsidence velocities of surface PS pixel targets for 2301, 2302 and 2304 working faces as 36mm/a, 52mm/s and about 90mm/a, respectively; and the average counterparts as 19mm/a, 23mm/a and 43mm/a, respectively. This result reveals larger subsidence speed in 2304 than the rest. The reasons for this phenomenon are: 1. Due to late exploitation, the underground strata in 2304 has yet achieved balance; 2. the mine exploration work in C incur a second disturbance in the strata in 2304.

The above solution-seeking for deformation velocity is founded on the premise that □V in equation (13) is linear. In order to acquire the deformation velocity at different time intervals, we assume that each time interval corresponds to one value of □V. On this basis, we calculate the integral of time dimension and subsequently obtain deformations in specified time spans. These deformations are superposed every 33 days to find the solutions of maximum subsidence. Then, the maximum subsidence velocity in each superposed timespan is obtained and plotted in Fig.8. According to the subsidence velocity in this figure, after the exploitation work is stopped, the tendencies of ground surface deformation in each working face during the observation period are coordinated, and all of the subsidence velocities are below 0.4mm/d. As can be seen from the changing trend, in spite of the slow subsidence, the subsidence velocities at different subsections of the observation period are periodically changing. The reason is that after roof caving above the goaf, broken rocks contact each other in different forms (point-point, point-plane, line-plane, and plane-plane). The temporal state of equilibrium is destroyed when the soil surrounding the hollows located beneath the contact surface is consolidated under the action of overlying rock stress. As the overlying rock moves and the ground surface subsidence is accelerated, a new state of stress balance is formed. This process will repeat nonstop until the rock is compacted, and thus the subsidence velocity varies in cycle time. According to Fig.8, the first decrease in subsidence velocity occurs at the time interval of 33 days, and the second one at the time interval of 66 days. The prolonged time interval reflects the reduction in holes between broken rocks and the prolonged rebalance time. As time passes by, the old goafs gradually return to the state of stableness.

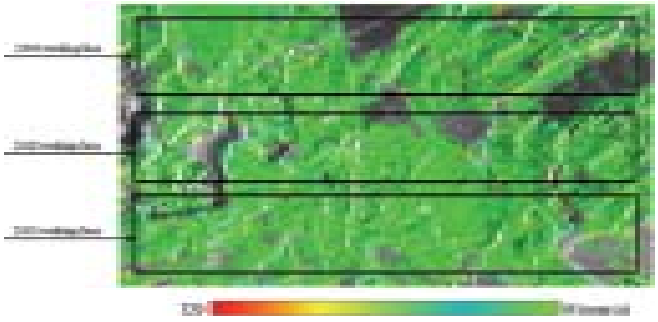

Fig.7 The enlarged drawing of subsidence velocity distribution of all PS pixels in the triple of old goafs

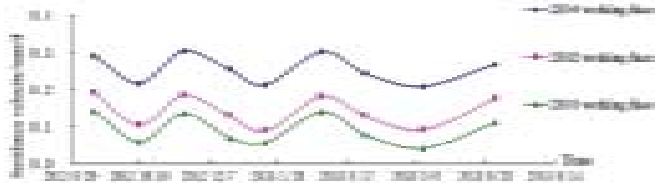

Fig.8 The maximum subsidence velocity in each superposed timespan

According to existing research findings, peak subsidence velocity and subsidence velocity increase with the increase of mining thickness under the influence of compacted broken rocks in residual old goafs. The larger the exploitation thickness is, the higher the rock to be broken is, and the larger the compacted space is, which corresponds to a faster ground surface subsidence. After the cease of mine exploration, the peak subsidence velocity is in positive proportion to mining thickness and in negative proportion to both the advance speed of working face and the mining thickness. By using existing data (Table 1), we use data fitting to obtain the residual relation between peak subsidence velocity and

TABLE 1. CHANGES OF GROUND SURFACE SUBSIDENCE VELOCITIES AFTER THE CEASE OF MINE EXPLOITATION IN DIFFERENT MINE AREAS

Observation station	Yangzhuang mine area	Renlou mine area	Zhangxiaolou mine area	Xinglong village mine area	Fengfeng mine area	Yuyang mine area
Exploitation height H/m	114	392.5	136	493	133	200
Exploitation thickness M/m	3.0	2.3	2.3	8.6	2.0	3.38
peak subsidence velocity Vm/mm/d	/	0.5	0.4	2.5	0.4	0.6773
depth-to-thickness ratio	38	170.6	59.13	57.33	66.5	59.17
Working face advance time c/m/d	1	1.64	0.68	3.57	1.46	4
Cycle time of subsidence velocity T/d	/	200	200	60	100	99

mining thickness, i.e., formula (20)), as well as the residual relation between the cycle time of subsidence velocity and H/M ,i.e., formula (21).

$$V_m = 0.3241M - 0.3089 \quad \text{... 20}$$

Where V_m is peak subsidence velocity, mm/d; M is mining thickness, m.

$$T = 1.4978\frac{H}{M} + 51.706 \quad \text{... 21}$$

Where T is the cycle time of subsidence velocity, d; H and M are the mining height and mining thickness, respectively, whose units are mÿc is the advance velocity of working face, m/d.

4. Conclusions

(1) We initiate the USB-based InSAR technology to monitor the residual ground surface subsidence in old goafs. A theoretical analysis is done on the selection criterion of USB interferometric pairs. We also expound PS pixel phase modeling and parameter estimation, on whose basis the USB InSAR method is employed towards the law of residual ground surface subsidence in three old goafs in Yulin mine areas.

We propose a serial approach to detect targeted PS pixels, i.e. by connecting time series parameters (including correction coefficients, amplitudes and amplitude discretion indices (ADIs)) in series to detect PS pixels more accurately. Specifically speaking, correction coefficients and amplitudes are first employed to exclude seriously decorrelated pixels and pixels of weak return signals; then, PS pixels are determined by ADIs according to the steadiness of pixel amplitude.

After the exploitation work is stopped, the tendencies of ground surface deformation in each working face during the observation period are coordinated, and all of the subsidence velocities are below 0.4mm/d. The first decrease in subsidence velocity occurs at the time interval of 33 days, and the second one at the time interval of 66 days. The prolonged time interval reflects it that as time passes by, the old goafs gradually return to the state of stableness.

We establish the empirical relation formula of peak subsidence velocity and mining thickness, and of the cycle time of subsidence velocity and H/M, which provides basis for predicting and evaluating the residual deformation in old goafs.

Acknowledgment

The author Chen B. Q. thanks the Basic Research Project of Jiangsu Province (Natural Science Foundation, No. BK20160218) and the research project of Jiangsu Normal University (No. 15XLR018) for the financial support.

References

[1] Wang Z. S., (2011): "Study on the non-linear theory of old goaf stability evaluation and its application," M.S. thesis, Dept. Xuzhou: China University of Mining and Technology, 68-69.

[2] Deng K. Z., Tan Z. X., Zhang H. Z., (2012): "Research on calculating method of residual subsidence of longwall goaf ," *Journal of China Coal Society*, vol. 37, no. 10, pp. 1601-1605.

[3] He G. Q., Yang L., Ling G. D., (1991): "Mining subsidence Theory,"in Xuzhou: *China University of Mining and Technology Press*, pp. 116-118.

[4] Juan Manuel BarrazaBurgos, Deisy ChavesSanchez, María Patricia TrujilloUribe, Francisco Javier VelascoCharria, Jaime José AcuñaPolanco, "Thermogravimetric characteristics and kinetics of pyrolysis of coal blends," *Revista de la Facultad de Ingeniería*, 2015, 30(4): 125-131.

[5] H. T. Zhang, J. P. Wei, Y. G. Wang, Z. H. Wen, B. H. Yao, "Application of Sampling Method Based on Negative Pressure Pneumatic Conveying in Soft Coal Seam,"*IJHT*, vol. 34, no. 3, pp. 473-478, Sept, 2016. DOI: 10.18280/ijht.340317.

[6] Zhang H. F. and Gao E. X. (2015): 3D numeracial simulation and influcing factors of loose top coal spontaneous combustion in roadway. *International journal of heat and technology*. [Online]. 33(3), pp. 91-96. Available:http://dx.doi.org/10.18280/ijht.330313.

[7] Han B. H., (2014): "Deep repairing for coal machinery equipment based on the remanufacturing," *Int J IIETA*ÿvol.1, no.1, pp. 21-26,. DOI: http://dx.doi.org/10.18280/amece.010105

[8] Li B., (2016): "Image Processing-based Quantitative Representation of Coal Porosity", *Revista de la Facultad de Ingeniería*, 31(5): 180-186.

[9] Jung H. C., Kim S. W., Jung H. S., (2007): "Satellite observation of coal mining subsidence by persistent scatterer analysis," *Engineering Geology*, vol. 92, pp. 1-13.

[10] Gueguen Y., Deffontaines B., Fruneau B., (2009): "Monitoring residual mining subsidence of Nord/Pas–de–Calais coal basin from differential and Persistent Scatterer Interferometry (Northern France)," *Journal of Applied Geophysics*, vol. 69, pp. 24-34.

[11] Fan H. D., Deng K. Z., Zhu C. G., (2012): "Deformation monitoring and prediction methods for expressway above goaf based on time series SAR technique," *Journal of China Coal Society*, vol. 37, no. 11, pp. 1841-1846.

[12] Liu X. F., Deng K. Z., Fan H. D., (2014): "Study of old goaf residual deformation monitoring based on D-

InSAR techniques," *Journal of China Coal Society*, vol. 39, no. 3, pp. 467-472.

[13] Rodriguez E., Morris C. S., Belz J. E, (2006): "A global assessment of the SRTM performance," *Photogrammetric Engineering & Remote Sensing*, vol. 72, no. 3, pp. 249-260.

[14] Gorokhovich Y., Voustianiouk A., (2006): "Accuracy assessment of the processed SRTM-based elevation data by CGIAR using field data from USA and Thailand and its relation to the terrain characteristics," *Remote Sensing of Environment*, vol. 104, no. 4, pp. 409-415.

[15] Liu G. X., Jia H. G., Nie Y. J., (2014): "Detecting Subsidence in Coastal Areas by Ultrashort-Baseline TCPInSAR on the Time Series of High-Resolution TerraSAR-X Images," *Geoscience and Remote Sensing, IEEE Transactions on*, vol. 52, no. 4, pp. 1911-1923.

[16] Liu G. X., Chen Q., Luo X. J., (2012): *The theory and method of permanent scatterer interferometric radar.* Beijing: Science Press,. pp.185-189.

[17] Ferretti A., Claudio P., Rocca A., (2001): "Permanent Scatters in SAR Interferometry," *IEEE Transactions on Geoscience and Remote sensing*, vol. 39, no. 1, pp. 8-20.

[18] Chen Q., Liu G. X., Li Y. S., (2006): "Automated Detection of Permanent Scatterers in Radar Interferometry: Algorithm and Testing Results," *Acta Geodaetica et Cartographica*, vol. 35, no. 2, pp. 112-117.

[19] Ferretti A., Prati C., F. Rocca, (2000): "Non-linear subsidence rate estimation using permanent scatters in differential SAR interferometry," *IEEE Transactions on Geoscience and Remote Sensing*, vol. 38, no. 5, pp. 2202-2212.

[20] Liu G. X., Buckley S. M., X. L. Ding, (2009): "Estimating spatiotemporal ground deformation with improved permanent-scatterer radar interferometry," *Geoscience and Remote Sensing, IEEE Transactions on*, vol. 47, no. 8, pp. 2762-2772.

[21] Zhang L., Ding X. L., Lu Z., (2011): "Modeling PSInSAR time series without phase unwrapping," *Geoscience and Remote Sensing, IEEE Transactions on*,vol. 49, no. 1, pp. 547-556.

[22] Hooper A., Zebker H.A., (2007): "Phase unwrapping in three dimensions with application to InSAR time series," *JOSA A*, vol. 24, no. 9, pp. 2737-2747.

[23] Chen Q., Ding X. L., Liu G. X., (2009): "Baseline recognition and parameter estimation of persistent-scatterer network in radar interferometry," *Chinese Journal of Geophysics*, vol. 52, no. 9, pp. 2229-2236.